Chemical Engineering Science: X 12 (2021) 100112

Contents lists available at ScienceDirect

Chemical Engineering Science: X

journal homepage: www.elsevier.com/locate/cesx

Computational particle fluid dynamics simulation of biomass gasification in an entrained flow gasifier

Ramesh Timsina *, Rajan K Thapa, Britt M.E. Moldestad, Marianne S. Eikeland

Department of Process, Energy and Environmental Technology, University of South-Eastern Norway, Kjølnes Ring 56, 3918 Porsgrunn, Norway

ARTICLE INFO

Article history:
Received 16 April 2021
Received in revised form 13 August 2021
Accepted 19 August 2021

Keywords:
Entrained flow
Biomass gasification
MP-PIC
CPFD
Clean energy

ABSTRACT

Entrained flow gasification is an established technology for coal and petroleum coke particles. The technology is being investigated extensively for biomass gasification to meet the requirement of the green energy targets. A three-dimensional computational particle fluid dynamics (CPFD) model is developed to simulate an Entrained Flow (EF) gasification reactor. The model is validated against experimental gas composition and process temperature reported from an experiment published in the literature. The interdependence between reactor hydrodynamics, thermal and reaction chemistry is demonstrated and described for an EF reactor. Simulations show zones of high and low temperatures suggesting different reaction zones, such as a partial combustion zone near the fuel injector followed by a gasification zone. Particles in the central region show high carbon conversion compared to the particles in the other zones. Char- O_2 and char-H_2O are significant in the gasifier entrance region, whereas the char-CO_2 reaction is prevalent throughout the reactor elevation. The optimal gasification performance (higher mole fraction of CO and H_2) is in the range of equivalence ratio 0.3 to 0.44.

1. Introduction

The world's energy consumption is ever-increasing, and the need for this energy to be environmentally friendly produced is increasingly important. Both on national and international levels, efforts are made to limit greenhouse gas emissions (IEA, 2019). For example, the European Union (EU) has set a target of 60% emission reduction to achieve carbon neutrality by 2050 (Voultsos et al., 2020). Bioenergy shared approximately 12.5% of the global energy demand in 2019, out of which 7.5 % is coming from the traditional biomass usage (Renewables 2020 - Global status report, 2020). Therefore, biomass is an important resource to replace the current consumption of fossil fuels (Bandara et al., 2018). Biomass gasification is a thermochemical conversion of carbonaceous fuels with the application of gasifying mediums such as air, steam, and oxygen. Gasification of biomass gives non-condensable gases such as carbon monoxide (CO), carbon dioxide (CO_2), hydrogen (H_2), methane (CH_4), higher molecular hydrocarbons (ethane, etc.), condensable vapors (tars) and solid residue (unconverted char and ash). Gasification and Integrated Gasification Combined Cycle (IGCC) is a promising option to improve the power generation efficiency from biomass. Lower emission of greenhouse gases, NO_X, and SO_X pollutants and low level of particulate emissions and market flexibility makes biomass gasification technology better as compared to conventional coal-fired power plants (Long et al., 2020).

Entrained Flow (EF) biomass gasifier is essentially a continuous flow reactor operated at elevated temperature (around 1400 °C) and pressure (20–70 bar) (Basu, 2018). Fuel, as well as the gasifying agent, are introduced concurrently into the reactor. Fuel particles typically have a very short residence time of 2–3 sec (Qin, 2012). Therefore, smaller particles of around a few hundred microns are needed to achieve a good heat transfer and mixing between the fuel particles and the gasifying agent (Guo, 2020). EF gasification has been an established technology for the coal and petroleum coke particles since 1950 (Duchesne, 2012), and the technology is being investigated extensively for biomass gasification to meet the requirements for reduced greenhouse gas emissions.

Several complex physical and chemical transformations occur over time and space in an EF gasifier. Particle movement and fluid flow play an important role in reactor hydrodynamics. The solid–gas flow in an EF reactor is characterized by a turbulent flow. Under ideal conditions, the residence time of the biomass particles lies within a few seconds giving a conversion efficiency as high as 99%. Reactor hydrodynamics, particle–particle collisions, char conversion, and fluid-particle mixing have a great impact on the gasification behavior of the EF gasifier. The conversion of biomass

* Corresponding author at: 50A, Vallermyrvegen, 3917 Porsgrunn, Norway.
E-mail addresses: ramesh.timsina@usn.no, timsinarames@gmail.com (R. Timsina).

https://doi.org/10.1016/j.cesx.2021.100112
2590-1400/

Nomenclature

Symbols	Description Unit
Δ	subgrid length [–]
A_v	pre-exponential factor [s^{-1}]
C_d	drag coefficient [–]
C_p	specific heat capacity (constant pressure) [J $K^{-1}kg^{-1}$]
C_V	specific heat capacity (constant volume) [J $K^{-1}kg^{-1}$]
C_s	Smagorinsky coefficient [–]
D_p	drag function [s^{-1}]
D_t	turbulent mass diffusivity [kg/(s.m^2)]
$\delta\dot{m}$	mass production rate [kg/s]
$\delta\dot{m}_{i,c}$	mass production rate from gas-phase reaction [kg/s]
E_v	activation energy [K^{-1}]
F	interphase momentum exchange rate per volume [N/m^3]
f	particle distribution function (PDF) [–]
g	acceleration due to gravity [m/s^2]
h	Enthalpy [J]
m	Mass [Kg]
$Nu_{g,s}$	Nusselt number [–]
P	Pressure [Pa]
Pr	Prandtl number [–]
P_s	constant [$Kgm^{-1}s^{-2}$]
$\dot{Q}$	energy source per volume [J/m^3]
$\vec{q}$	gas heat flux [J/m^3]
$\dot{q}_D$	enthalpy diffusion rate [J/m^3]
r	particle radius [m]
Re	Reynolds number [–]
S_h	conservative energy exchange [J]
Sc	Schmidt number [–]
T	Temperature [K]
t	time [s]
u	velocity [m/s]
$\vec{u}$	velocity (vector) [m/s]
v	velocity [m/s]
$Y_{g,i}$	mass fraction of each fluid species [–]

Greek letters

β	constant [–]
ε	constant [–]
ρ	density [Kg/m^3]
λ	thermal conductivity [J/(s.m.K)]
τ	stress [N^2/m^2]
μ	viscosity [kg/(m.s)]
φ	viscous dissipation [J]
α	volume fraction [–]
$k-\varepsilon$	k -epsilon [–]

Subscripts

g	gas phase
p	particle phase
i	species

depends upon the characteristics of the biomass, pressure, temperature, heat, and mass transfer inside a reactor. The characteristics of biomass include its shape and size and the amounts of fixed carbon, volatiles, moisture, ash, and calorific value. The char reactivity and the amount of char affect the product gas compositions (Bikane et al., 2020; Thapa & Halvorsen, 2014. Traditionally established monitoring systems (thermocouples, gas chromatography, etc.) are usually too slow to respond to a sudden change in process condition and could challenge the plant security (Sepman et al., 2017).

As the gasifier operates at high temperatures, the problems related to ash and tar formation during biomass gasification are minimal, giving high-quality syngas (CO, H_2). Reformation of tars into light hydrocarbons such as CH_4, C_2+, etc. occurs at a temperature above 1100 °C (Llamas et al., 2020). EF gasifiers are designed to work in slagging mode, where the variation in the ash melting point is less problematic as long as the operating temperature exceeds the slag fluid temperature. EF gasifiers have fuel flexibility because of their slagging mode operation. EF gasifiers have high carbon conversion efficiency as compared to fluidized bed gasifiers (Weiland et al., 2013).

The challenges associated with EF gasifiers are energy efficiency, heat recovery from the product gas, the durability of the systems, short residence time, fouling (slagging behavior), and installation costs. Pretreatment of the particles to a suitable size requires a significant amount of energy and costs. The suitable choice of milling techniques or fuel treatment (torrefaction or pyrolysis) can increase the total process efficiency (Weiland et al., 2013). Less reactive products such as soot and char formed during the gasification process limit the complete conversion of biomass. For an EF gasifier to be cost-competitive, especially industrial-scale applications, understanding various aspects of entrained flow gasification is imperative. Therefore, modeling and simulation of such systems have become necessary for a better understanding of the gasification process in a short time frame with a low cost.

The hydrodynamics and the reaction kinetics are quite complex in an EF reactor. Simulation using computational fluid dynamics is becoming an important tool to study these parameters. The current study focuses on the numerical simulation of the gas–solid flow with heat transfer and the chemical reactions inside an EF reactor. To achieve this goal, a CPFD model is developed for the Pressurized Entrained Flow Biomass Gasification plant (PEBG) designed, developed, and operated by Weiland et al. at the Energy Technology Centre (ETC) in Piteå, Sweden (Weiland et al., 2013). The CPFD numerical scheme incorporates the Multi Phase Particle-In-Cell (MP-PIC) modeling approach (Andrews & O'Rourke, 1996; Snider et al., 2011).

1.1. CFD modeling of EF gasifiers

Biomass gasification in an EF reactor involves different thermodynamic domains and complex reactions. Experimental optimization of the EF gasifiers is difficult and challenging (i.e., optimization of geometry, feeding positions, etc.). Therefore, simulation tools are becoming imperative and valuable tools for the study and for the process optimization towards the desired downstream applications. Computational Fluid Dynamics (CFD) models of such systems in plant scale have become practical due to the development of computer power and efficient numerical algorithms. CFD models are capable of simulating the effects of different operational parameters such as pressure, temperature, equivalence ratio, etc. (Chiesa et al., 2005; Gungor & Yildirim, 2013). The effect of different biomass feedstock, particle sizes, geometry, etc., can be evaluated with respect to the product gas compositions and LHV.

Modeling of multiphase flow systems in an EF is challenging due to the coupling of turbulent gas flow and particle motions.

Other challenges include the difficulties in modeling the momentum exchange between the phases, interparticle forces such as van der Waals forces, electrostatic forces, inter-particle collisions, and the difference in size, shape, and densities of the particles in the solid phase. In addition to these, the gasification of biomass possesses challenges related to the thermal model, devolatilization model, heterogeneous reactions, etc. (Bandara et al., 2018; Timsina et al., 2020).

The basic approaches to model gas–solid multiphase systems are the Eulerian-Eulerian (EE), and the Eulerian-Lagrangian (EL) approaches. The details of these approaches can be found in the literature (Thapa, 2015). The CPFD methodology follows the MP-PIC modeling approaches. MP-PIC approach is based on the EL approach, which introduces the concept of computational particles (parcels), where particles with similar properties such as size, density, residence time, velocity, etc., are grouped into a computational particle. Parcels are modeled in a discrete frame and the particle interactions are calculated on the Eulerian frame. The inter-particle stresses are calculated by an isotropic solid stress function and then interpolated back to the individual particles (Bandara et al., 2018). The fluid phase is solved with an Eulerian approach. The CPFD platform is developed from the MP-PIC modeling approach. The strong coupling between the fluid and the particle phases gives a high level of accuracy and fast computational time in CPFD modeling. MP-PIC employs a simple particle-'pressure' model that prevents particle from becoming closely packed and eliminates the need to track the collision of the particles directly (Mu et al., 2020; Verma & Padding, 2020). Intel(R) Core (TM) i7-8700 K CPU @ 3.70 GHz processor and Barracuda VR® 20.0.0 version were used to simulate the developed model.

The CPFD model has been successfully applied for reactors operating with a dilute flow of solid particles, where the gas–solid behavior is similar to that in an EF reactor. For example, risers of the circulating fluidized bed (Shi et al., 2015; Wang et al., 2015), downer of the circulating fluidized bed (Yingya Wu et al., 2020), downer reactor (Abbasi et al., 2013), downflow reactor (Lanza et al., 2016), cement calciners (Nakhaei et al., 2021; Nakhaei et al., 2018; Nakhaei et al., 2019) and pneumatic conveying system (Ariyaratne et al., 2017) has been modeled in CPFD platform. Besides, Liang et al. (Liang et al., 2020) have developed a CPFD model for an EF gasification reactor, and their results are discussed in Section 1.2.

The number of grid elements in a modeled geometry is important since it affects both the accuracy and the time it takes to simulate a process. A bulk flow region can be modeled with a coarse grid; however, a finer grid gives better results in areas with high gradients of temperature, pressure, concentrations, etc. The software package uses grid resolution only in Cartesian coordinates and it is possible to define a finer grid at a particular region. It is important to note that the grid generation should be performed carefully to capture every small part as it may affect the bed hydrodynamics significantly. The grid resolution was changed accordingly until the convergence of the simulation results with a reasonable simulation time was achieved. The effects of grid size on cell averaged particle properties are presented in Fig. 1. Coarse grid misrepresents the particle structure, whereas the finer grids lead to high computational costs.

1.2. Previous works

A number of studies have developed a CFD model (based on EL modeling) for EF reactors because of the wide applicability and versatility. However, most of the authors have modeled the EF reactor based on coal gasification (Abani & Ghoniem, 2013; Chen et al., 2012; Eluk et al., 2017; Kumar & Ghoniem, 2013; Yuxin Wu et al., 2010; Ye & Ryu, 2015). This section provides a brief overview of the recent previous works performed on the CFD simulation of an EF biomass gasification reactor.

The effect of reactor temperature, excess air ratio, steam/carbon ratio, gasifying medium, reactor structure, and feedstock properties are reported in (Ku et al., 2014; Ku et al., 2019). Ku et al. have shown a positive effect on both the H_2 and CO productions, increasing the reactor temperature. Increasing the excess air ratio decreased both H_2 and CO production, and increasing the steam/-carbon ratio increases the H_2 production but decreases the CO production (Ku et al., 2014). The introduction of O_2 improved CO production and carbon conversion, whereas an excessive use of O_2 gave a reduced combustible gas yield and Cold Gas Efficiency (CGE). H_2 production, carbon conversion, and lower heating value rose after steam addition. Biomasses with a higher fixed carbon or volatile content and a lower moisture content gave a high combustible gas yield (Ku et al., 2019).

Gao et al. (Gao et al., 2018; Gao et al., 2016) have investigated the relative error of the developed model with the experimental results. A finite rate/eddy dissipation model was applied to calculate the reaction rates for homogeneous phase reactions and an intrinsic reaction rate model was used with user-defined functions (UDFs) to calculate char reaction rates. The relative error for LHV, gas production, CGE, and carbon conversion efficiency are within the ranges of 1–13%, 1–8%, 1–12%, and 1–11%, respectively (Gao et al., 2016). The relative errors between the simulated and experimental gasification performances were in the ranges of 9.6–23.3% (gas heating value), 1.2–5.9% (gas production), and 9.8–16.6 (carbon conversion efficiency) (Gao et al., 2018). The authors have also proposed/developed the reaction rate kinetics for char-CO_2 and char-O_2 reactions.

Guo et al. (Guo et al., 2020) have developed an EL CFD model in OpenFOAM to study particle hydrodynamics, heat transfer, and devolatilization kinetics. A total of four different approaches were tested for the quantitative comparison analyses. The spheroidal particle shape assumption with adjusted spheroidal surface area and the Kishore-Gu model proves to favor the drying and devolatilization process. However, the sphere and simplified non-sphere model predict 61% and 43% longer residence times, respec-

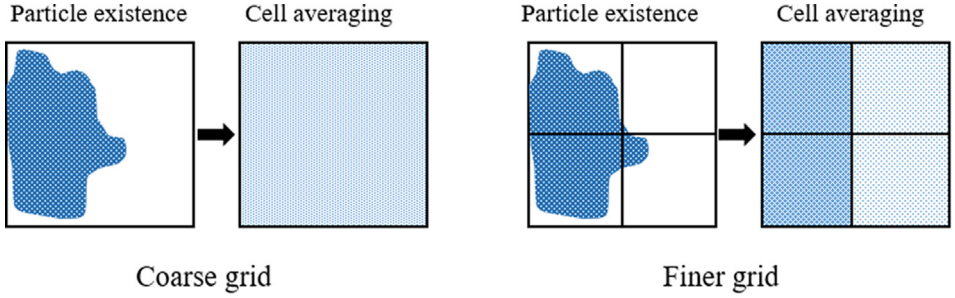

Fig. 1. Effect of grid size for cell averaged particle properties. The demonstration shows that cell averaging affects the particle concentration after cell averaging.

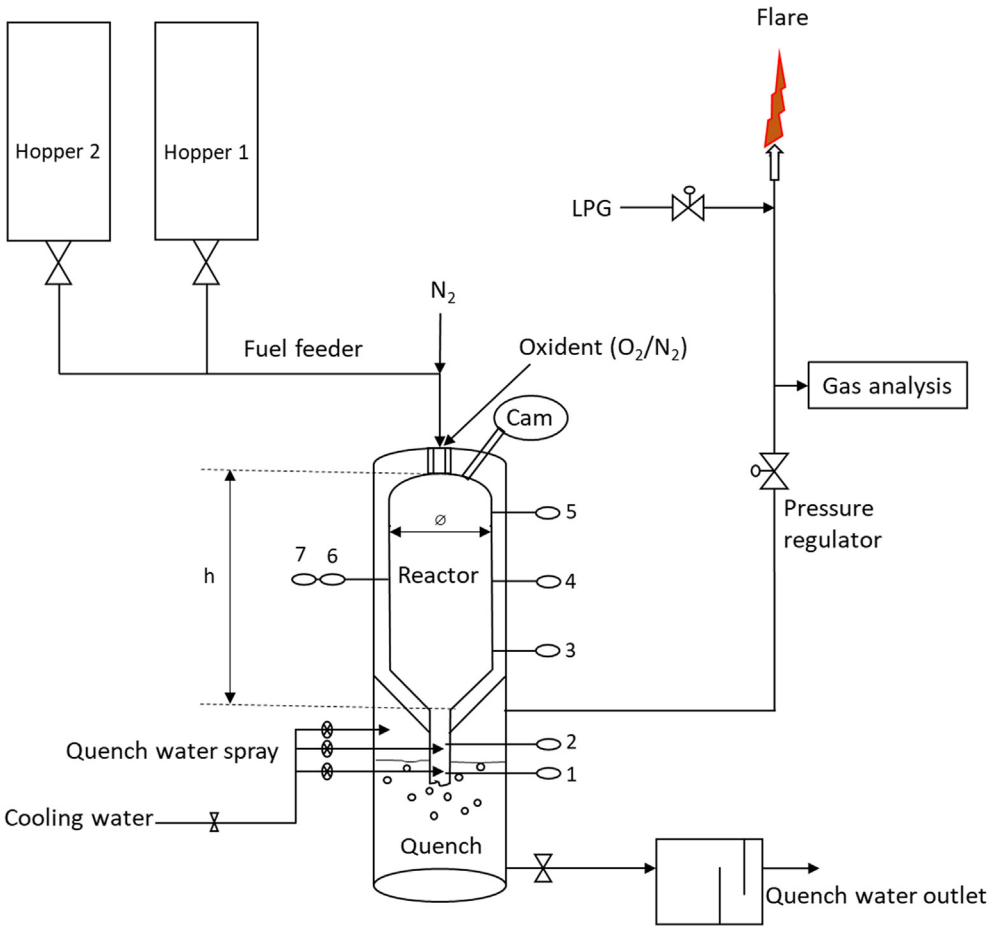

Fig. 2. Schematic process flow diagram of the PEBG plant adapted from (Weiland et al., 2013). Numbers (1–7) represent the thermocouples to monitor the temperature and pressure. The height (h) and the inner diameter (∅) are 1.67 m and 0.52 m, respectively.

tively, than the spheroid models, and the longer residence time seems to favor the char conversion process (Guo et al., 2020).

Liang et al. (Liang et al., 2020) have developed a CPFD simulation model for an EF gasification reactor for the Utah Bituminous coal. The detailed particle information and residence time were studied. The rapid expansion from a tracer injector and fast reactions play an important role in forming the particle distribution zone in the gasifiers. The authors pointed out that due to the complexity of the EF gasification reactions and the computational power limitation, the models were often simplified to two-dimensional or semi three-dimensional models. There was also limited information available in the literature about the particle temperatures, carbon contents, and locations for the discrete particles (Liang et al., 2020).

In view of these paper, this study aimed at giving detailed information about particle hydrodynamics, the temperature distribution inside the reactor, gas composition, reaction rates, and kinetics. This gives a better understanding of the reactor hydrodynamics and the transient behavior of the reactor, which is crucial at the industrial scale investments. To the best of the author's knowledge, no previous studies of reaction rate kinetics for EF reactors are available in the literature.

2. Experimental and CPFD model setup

The experimental studies were performed by Weiland et al. (Weiland et al., 2013). Fig. 2 shows the experimental setup located at the Energy Technology Centre (ETC) in Piteå, Sweden. The reactor diameter and height are 52 cm and 167 cm, respectively. The reactor has a conical-shaped outlet followed by a water sprayed quench bath for gas cooling and particle separation. Biomass stored in the hopper is fed at the top of the reactor along with O_2 and N_2. A quench bath maintains the system temperature and cools down the product gas out from the reactor. The details of the reactor can be found in the study of Weiland et al. (Weiland et al., 2013). The operating conditions of the reactor and the feed definition are shown in Table 1. For safety reasons, the gasifier was operated at pressure $\leq$ 2 bar.

The proximate and the ultimate analysis of the stem wood powder are shown in Table 2.

A CPFD model was developed in Barracuda to simulate biomass gasification in an EF reactor. A three-dimensional geometric model (cylinder with conical outlet) developed in AutoCAD was imported into the model. The geometry was meshed using the built-in mesh

Table 1
The experimental test conditions operated by Weiland et al. (Weiland et al., 2013).

Fuel feeding rate (kg/h)	40
Total N_2 inlet (kg/h)	15.1
O_2 inlet (kg/h)	27
O_2 inlet concentration	89
Oxygen equivalence ratio	0.49
System pressure (bar)	1.95
Desired process temperature (°C)	1200

Table 2
Ultimate and proximate analysis of the biomass.

Proximate analysis (wt.%, wet basis)		*Ultimate analysis (wt.%, dry basis)*	
Fixed Carbon	14.4	Ash	0.4
Volatiles	80.5	C	50.9
Moisture	4.7	H	6.3
Ash	0.4	N	0.10
		S	0.006
		Cl	0.02
		O (calculated)	42.4

Table 3
Particle phase model parameters and their values.

Fluid drag model	Wen-Yu
Close pack volume fraction	0.2
Maximum momentum redirection from collision	40%
Normal to wall momentum retention	0.15
Tangent to wall momentum retention	0.85
Pressure constant in the particle stress model	1
Initial time step	0.0001 s

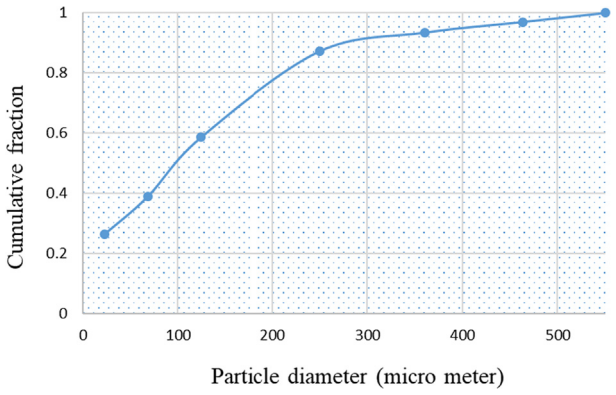

Fig. 3. Particle size distribution.

generator with a uniform grid option. A total of 193,167 computational cells were chosen for the current study. The model is validated against the experimental gas composition reported by Weiland et al. (Weiland et al., 2013). The Wen-Yu drag model was selected and the particle model parameters used in the model are presented in Table 3.

Modeling of an EF reactor commonly neglects particle–particle interactions as the reactor operates at lower solid fractions. However, particle–particle interactions play an important role around the fuel injector. Particle-particle interaction in the model can be altered by altering the close pack volume fraction and the maximum momentum redirection from particle collisions. In addition, the Blended Acceleration Model (BAM) was activated as the particle mixture was composed of a broad range of particle sizes (25–550 μm). BAM blocks the unrealistic particle segregation by absorbing the sustained particle contact (Bandara et al., 2021). The particle size distribution of the biomass feed is illustrated in Fig. 3.

The boundary conditions and the computational mesh of the developed model are shown in Fig. 4. Biomass and the fluidizing agent were implemented as an injection boundary. In the model, particle inflow should be assisted by a fluid stream and the flow can be manipulated by changing the 'slip velocity' option. However, an injection boundary was chosen for the introduction of particles into the reactor because it does not need the assistance of a fluid stream. The red triangles with spheres at the top represent the injection points. Totally 20 injection points along the circle and one at the middle were defined in the model.

Two flux planes were defined at the entrance and the reactor's exit to monitor the flow into and out of the reactor. Also, seven intermediate planes were defined to monitor the flow rate and the gas composition at approximately 20 cm apart. A pressure boundary (yellow plane) was defined at the bottom of the reactor to allow outflow of the product gas and the solid materials. The CPFD platform includes the model for both gas-solids and gas-wall heat transfer as well as the radiation between a thermal wall and particle-phase only. The user can choose a drag model from the available built-in drag models or can create a drag model of user choice.

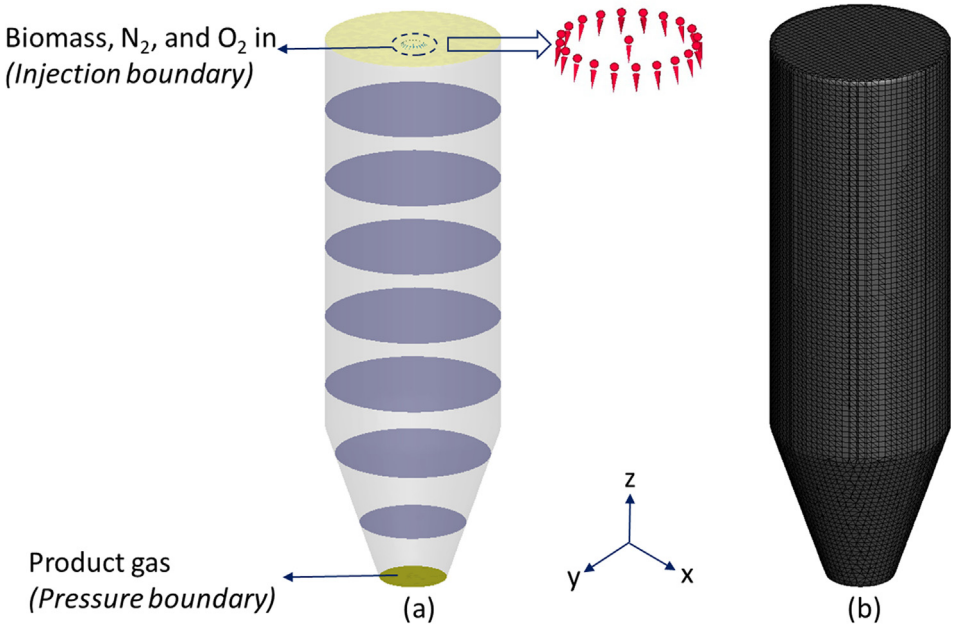

Fig. 4. (a) – Boundary conditions, (b) – computational grid. The planes in the left figure show the data capturing planes. The three-dimensional geometry was imported in the CPFD model and mesh was generated using an in-built mesh generator.

Chemical reactions are an integral part of many industrial applications and are closely coupled with the fluid-particles dynamics and the heat and mass transfer inside a reactor. The reactor temperature affects the reaction rates and thereby affecting the reactor heat transfer and the reactor hydrodynamics. Heterogeneous reactions produce or consume gases from solids affecting the total gas volume, which changes the reactor hydrodynamics. There can be thousands of reactions in any industrial chemical process and it is impossible to solve a large number of coupled reactions over a hundred seconds of simulation time. Thus, a common consensus is to postulate a limited set of reactions describing the major conversion inside the reactor, which makes computational tracking easy (Snider et al., 2011).

Devolatilization of the biomass is the first step in a biomass gasification process. Biomass particles are subjected to fast heating rates with short residence times. The devolatilization kinetic parameters are taken from the study of Guo et al. (Guo et al., 2020) as follows:

$$\frac{dm_{devol}}{dt} = -\mathrm{A}\exp\left(-\frac{E}{T_p}\right)m_{devol} \tag{1}$$

Where, m_{devol} is the remaining volatile in the particle (kg) and t is time (s), A is a pre-exponential factor ($18.9 \times 10^3\ s^{-1}$), E is the activation energy ($2562.4\ K^{-1}$) and T_p is the particle temperature (K). In order to simplify the model, the formation of tar and other higher molecular hydrocarbons was neglected. Based on the literature data, volatiles count as 80% on a dry basis, and the remaining is char and ash after the devolatilization. The major reactions together with the kinetics are presented in Table 4. As the chemistry module was implemented as volume average chemistry, the temperature for the heterogeneous reactions was taken as a weighted average with 50% of the average particle temperature and 50% of the cell's gas temperature. The particles for the EF reactor are small enough, which does not add much uncertainty due to this assumption. m_s is the mass of carbon which gives the approximate amount of char components.

$$m_s = M_{wC} \times [\mathrm{C(s)}]$$

M_{wC} is the molecular weight of carbon, and [C(s)] is the molar concentration of solid carbon.

The time step for a transient model is an important parameter. It is important that the time step is small enough to represent any rapidly changing variables of interest. However, if the time step is too big, an accumulation of errors will occur (Zhang et al., 2000). To solve this problem, a varying time step can be utilized with the help of the Courant-Friedrichs-Lewy (CFL) number:

$$\mathrm{CFL} = \frac{v\Delta t}{\Delta x_{cell}} \tag{2}$$

$v$is velocity, Δt is time step and Δx_{cell} is cell size. The default minimum and maximum values of CFL in the model are 0.8 and 1.5, respectively, which gives stability for the numerical solver.

2.1. Governing equations

The gas phase mass and momentum conservation equations are given by the continuity and the Navier-Stokes equations represented by Equations (3) and (4) respectively.

$$\frac{\partial\left(\alpha_g\rho_g\right)}{\partial t} + \nabla\cdot\left(\alpha_g\rho_g\vec{u}_g\right) = \delta\dot{m}_p \tag{3}$$

$$\frac{\partial}{\partial t}\left(\alpha_g\rho_g\vec{u}_g\right) + \nabla\cdot\left(\alpha_g\rho_g\vec{u}_g\vec{u}_g\right) = -\nabla p + F + \alpha_g\rho_g g + \nabla\cdot\left(\alpha_g\tau_g\right) \tag{4}$$

where α, ρ and $\vec{u}$ represent the volume fraction, density, and velocity vector respectively. $\delta\dot{m}_p$ is the gas mass production rate per volume formed from the particle-gas chemical reaction. In the case of the cold flow model with no chemical reaction, $\delta\dot{m}_p$ becomes zero. P is the mean flow gas pressure, g is the acceleration due to gravity, τ_g is the fluid phase stress tensor and F is the inter-phase momentum transfer rate per unit volume (particle to fluid phase).

For a Newtonian fluid, the gas phase stress tensor for each species, τ_g is given by:

$$\tau_{g,ij} = \mu\left[\left(\frac{\partial u_i}{\partial x_j} + \frac{\partial u_j}{\partial x_i}\right) - \frac{2}{3}\mu\delta_{ij}\frac{\partial u_k}{\partial x_k}\right] \tag{5}$$

where μ is the shear viscosity, which is the sum of the laminar shear viscosity and the turbulence viscosity defined in the Smagorinsky turbulence model (Smagorinsky, 1963). The model is given in Equation (6) (Snider et al., 2011).

$$\mu_t = C_s\rho_g\Delta^2\left(\frac{\partial u_i}{\partial x_j} + \frac{\partial u_j}{\partial x_i}\right) \tag{6}$$

The Smagorinsky coefficient $C_s$has a default value of 0.01. Δ and is the subgrid length and is given by:

$$\Delta = (\delta x\delta y\delta z)^{1/3} \tag{7}$$

A fluid-phase transport equation is solved for each gas species. The calculation of the fluid phase properties is based on the mass fraction $Y_{g,i}$ of the gas species making up the fluid mixture. $\delta\dot{m}_{i,c}$ is a chemical source term, which is the mass transferred between the gas species by the dissociation and the association of the chemical bond.

$$\frac{\partial}{\partial t}\left(\alpha_g\rho_g Y_{g,i}\right) + \nabla\cdot\left(\alpha_g\rho_g Y_{g,i}\vec{u}_g\right) = \nabla\cdot\left(\alpha_g\rho_g D_t\nabla Y_{g,i}\right) + \delta\dot{m}_{i,c} \tag{8}$$

D_t is the turbulent mass diffusivity and can be calculated from Equation (9). Sc is the Schmidt number in Equation (9). The standard value of the turbulent Schmidt number is 0.9 (Snider et al., 2011).

$$\mu/(\rho_g D_t) = \mathrm{Sc} \tag{9}$$

Table 4
Reactions and kinetics.

Reaction	Reaction rate: r (mol.m^{-3}.s^{-1})	Reference
$C(s) + 0.5O_2 \rightarrow CO$	$2.51 \times 10^{-3} m_s T \exp(\frac{-8996}{T})[O_2]$	(Ku et al., 2014)
$H_2 + 0.5O_2 \rightarrow H_2O$	$5.69 \times 10^{14} exp(\frac{-17610}{T})[H_2][O_2]^{o5}$	(Bates et al., 2017)
$CH_4 + 1.5O_2 \rightarrow CO + 2H_2O$	$5.01 \times 10^{14} exp(\frac{-24357}{T})[CH_4]^{o}\square[O_2]^{08}$	(Bates et al., 2017)
$CO + H_2O \rightarrow CO_2 + H_2$	$7.68 \times 10^{10} exp(\frac{-36640}{T})[CO]^{05}[H_2O]$	(Snider et al., 2011)
$C(s) + CO_2 \rightarrow 2CO$	$1.272 m_s T exp(\frac{-22645}{T})[CO_2]$	(Snider et al., 2011)
$C(s) + H_2O \rightarrow CO + H_2$	$1.272 m_s T exp(\frac{-22645}{T})[H_2O]$	(Snider et al., 2011)

The energy conservation equation of the gas phase is:

$$\frac{\partial}{\partial t}\left(\alpha_g \rho_g h_g\right) + \nabla \cdot \left(\alpha_g \rho_g h_g \vec{u}_g\right) = \alpha_g \left(\frac{\partial P}{\partial t} + \vec{u}_g \cdot \nabla P\right) + \varphi - \nabla \cdot \left(\alpha_g \vec{q}\right) + \dot{Q} + S_h + \dot{q}_D + q_{wp} \quad (10)$$

where h is the enthalpy and q_{wp} is the radiative heat transfer between the thermal wall and the particle phase. The viscous dissipation (φ) and the energy source per unit volume ($\dot{Q}$) are neglected in this work. S_h is the conservative energy exchange from the particle phase to the gas phase. $\dot{q}_D$ is the enthalpy diffusion term and $\vec{q}$ is the gas heat flux. The expressions for the $\vec{q}$ and $\dot{q}_D$ are given as:

$$\vec{q} = \lambda_g \nabla T_g \quad (11)$$

$$\dot{q}_D = \sum_{i=1}^{N} \nabla \cdot \left(h_i \alpha_g \rho_g D \nabla Y_{g,i}\right) \quad (12)$$

where λ is the thermal conductivity calculated as a sum of a molecular conductivity (λ_m) and an eddy-conductivity (λ_t) from Reynolds stress mixing theory. The eddy-conductivity is calculated from the turbulent Prandtl number correlation.

$$Pr_t = (C_p \mu_t)/\lambda_t \quad (13)$$

The mass, momentum, and energy conservation equations are solved for the gas mixtures. The gas mixture properties are based on the mass fractions of the gas species calculated using Equation (8). The flow is considered compressible and the gas phase temperature, pressure, enthalpy, density, and mass fraction are correlated through the equation of state. CPFD uses the ideal gas equation of state.

The gas mixture enthalpy (h_g) is the sum of individual gas enthalpy (h_i), given by:

$$h_g = \sum_{i=1}^{N} Y_{g,i} h_i \quad (14)$$

$$h_i = \int_{T_o}^{T_g} C_{p,i} dT + \Delta h_{f,i} \quad (15)$$

where $\Delta h_{f,i}$ is the enthalpy of formation of species i at the reference temperature T_o. $C_{p,i}$ is the specific heat capacity of species i.

The gas-phase equations contain a source term and the mass, momentum, and energy are conserved between the phases. The gas chemistry does not change the mixture's total mass and enthalpy; however, with the gas–solid reactions, mass, momentum, and energy are transferred to the gas phase by chemical conversion of solids to gas. This is known as the interphase momentum transfer rate per unit volume (F) in Equation (4).

The dynamics of the solid particles are calculated by solving a transport equation for the Particle Distribution Function (PDF), f. The details of the transport equation can be obtained from the literature (Andrews & O'Rourke, 1996; Thapa et al., 2016). PDF is a function of particle spatial position $\vec{x}_p$, particle velocity $\vec{u}_p$, particle mass m_p, particle temperature T_p, and time t. Therefore, $f\left(\vec{x}_p, \vec{u}_p, m_p, T_p, t\right) d\vec{u}_p dm_p dT_p$ is the average number of particles per unit volumes with masses in the interval $(m_p, m_p + dm_p)$, velocities in the interval $(\vec{u}_p, \vec{u}_p + d\vec{u}_p)$ and temperature in the interval $(T_p, T_p + dT_p)$.

The particle velocity and acceleration are given by:

$$\frac{\partial}{\partial t}\left(\vec{x}_p\right) = \vec{u}_p \quad (16)$$

$$\frac{\partial}{\partial t}\left(\vec{u}_p\right) = D_P\left(\vec{u}_g - \vec{u}_p\right) - \frac{\nabla P}{\rho_p} + g - \frac{\nabla \tau_p}{\rho_p \alpha_p} + F_p \quad (17)$$

The particle volume fraction in Equation (17) is given by:

$$\alpha_p = \iiint f \frac{m_p}{\rho_p} dm_p d\vec{u}_p dT_p \quad (18)$$

where, D_P is the drag function which depends upon the particle size, position, velocity, and time. τ_p is the particle normal stress given by Equation (19). Particle interactions (particle to particle collisions) are modeled with the particle normal stress developed by Harris and Crighton (Harris & Crighton, 1994). The particle stress is derived from the particle volume fraction, which in turn is calculated from particle volumes mapped to the grid. Particle normal stress gives an approximation of the collective effects of all the neighbor particles of a particle. The CPFD method calculates the spatial gradients on an Eulerian grid and applies the gradient to discrete particles. The gradient in the particles accelerates the particle, which prevents the particle volume fraction from exceeding their close-pack volume faction. The particle pressure is a function of solid volume fraction and becomes zero when the solid volume fraction becomes zero (Snider et al., 2011).

$$\tau_p = \frac{P_s \alpha_p{}^{\beta}}{\max[(\alpha_{cp} - \alpha_p), \varepsilon(1 - \alpha_p)]} \quad (19)$$

Solid collisions depend upon the solid concentration and the solid velocity. Particle normal stress is exerted to a solid up to the point where the solid reaches the particle-mean velocity (Snider et al., 2011). P_s is a constant (Pa), α_{cp} is the particle volume fraction at close packing, β is a constant (between 2 and 5) and ε is a very small number in the order of 10^{-8}.

The fluid mass source in Equation (3) is given by:

$$\delta \dot{m}_p = \iiint f \frac{dm_p}{dt} dm_p d\vec{u}_p dT_p \quad (20)$$

where the time-rate change of particle mass dm_p/dt is the rate of change of the particle mass-producing gases through chemical reactions and is given by:

$$\frac{dm_p}{dt} = \frac{\alpha_g M w_c}{\alpha_p \rho_p} m_p \frac{d[C(s)]}{dt} \quad (21)$$

The interphase momentum transfer (F) in Equation (4) is given by:

$$F = \iiint f \left[m_p \left\{D_P\left(\vec{u}_g - \vec{u}_p\right) - \frac{\nabla P}{\rho_p}\right\} + \vec{u}_p \frac{dm_p}{dt}\right] dm_p d\vec{u}_p dT_p \quad (22)$$

The conservative energy exchange term S_h in Equation (10) from the particle phase to the gas phase is given by (Snider et al., 2011):

$$S_h = \iiint f \left[m_p \left\{D_P\left(\vec{u}_p - \vec{u}_g\right)^2 - C_V \frac{dP_p}{dt}\right\} - \frac{dm_p}{dt}\left\{h_p + \frac{1}{2}\left(\vec{u}_p - \vec{u}_g\right)^2\right\}\right] dm_p d\vec{u}_p dT_p \quad (23)$$

where, h_p is the particle enthalpy and C_V is the specific heat of the particle. The lumped heat equation for the particle is:

$$C_V \frac{dT_p}{dt} = \frac{1}{m_p} \frac{\lambda_g Nu_{g,s}}{2 r_p} A_s \left(T_g - T_p\right) \quad (24)$$

where $Nu_{g,s}$ is the Nusselt number for heat transfer from gas to the particle phase, m_p is the particle mass and r_p is the particle radius.

The radiative heat transfer between the thermal wall and the particle phase in the equation is given by:

$$q_{wp} = A_w F_{wp} \varepsilon_{wp} \sigma \left(T_w{}^4 - \bar{T}_p{}^4 \right) \quad (25)$$

where A_w is the area of the thermal wall, T_w is the wall temperature, $\bar{T}_p$ is the average particle temperature in a cell, F_{wp} is a view factor, σ is the Stefan-Boltzmann constant and ε_{wp} is the emissivity between the wall and particles in the cell.

In multiphase simulations, drag models are very important for predicting hydrodynamics. The model calculates a force acting on a particle as a function of the particle and fluid properties and the flow conditions. The details of the drag force and its expressions together with the numerical scheme for the CPFD approach are presented in the supplementary material.

3. Results and discussion

A pilot-scale EF gasifier is simulated with a CPFD scheme for the particle dynamics. The computation is three-dimensional non-isothermal with heterogeneous and homogeneous gasification chemistry. The gasification process itself is a complex process involving interactions between the solid flow, gas flow, and the chemical reactions in a thermal environment. Simulations were carried out for 100 s and the gas compositions, temperature, residence time, chemical kinetics, and mass flow rate were monitored. The average gas compositions were taken as the time average of the final 20 s of simulation. A detailed description of the simulation results at the initial reactor temperature of 1200℃ is presented in Section 3.1.

3.1. Simulation results at 1200 °C reactor temperature

Validation of a CFD model is an important aspect during the study of the simulation results. Table 5 shows the comparison between the experimental and simulation results. The mole percentage of CH_4 in the experiment also includes the mole percentage of C_2H_2 (0.3) and C_2H_4 (0.1). The simulation results agree reasonably well with the experimental data.

As the reactor hydrodynamics is concerned, the reactor is desired to have a uniform mixing between the fuel particles and the fluidizing agent. Fig. 5 shows the instantaneous particle distribution after 50 s. Particle scale information is captured by the Lagrangian tracking of solid particles. As depicted in Fig. 5 (a), particle temperature in the central region is lower, with particles flowing downward. This is due to most particles following the central path where a significant number of reactions (endothermic) occurs compared to the peripheral region. This also leads to the shorter residence time for the particles flowing through the central region, as shown in Fig. 5 (b). Particles in the central region of the gasifier have the lowest residence time (high speed), whereas the particle towards the outer region has high residence time (low speed). The particle species with longer residence time are the particles that undergo recirculation, expansion along the radial direction. Fig. 5 (c) shows the particle radius, which shows the near-uniform distribution of the particle with respect to size. The particle temperature, as well as the residence time, is highly related to the carbon conversion of the particles. Fig. 5 (d) shows the particle carbon content (mass fraction) for the simulated gasifier. Particle carbon content is lower in the central region and higher in the other region. Even with the lower residence time, carbon conversion is higher in the central region, which indicates that the higher residence time may not always result in higher carbon conversion.

Particle carbon content determines the char conversion for the process. Char conversion depends on the reactor conditions as well as the residence time of the fuel particle. Therefore, it is important to analyze the residence time of the solid particles inside the gasifier. Fig. 6 (a) shows the average residence time for all the particles. After the reactor reaches the steady state, the residence time stabilizes around the median value. The different values for the residence time are due to the fact that all the particles do not follow the same path inside the reactor. Some particles circulate back into the top peripheral corner giving the largest residence time, while particles following a straight(ish) path have a lower residence time.

As depicted in Fig. 6 (b), most of the particles (48.1%) have a residence time of 1.38–1.48 s. The rightmost column gives the distribution of the particles having a residence time greater than 1.68 s. The highest residence time recorded was 3 s at the start of the simulation process. It took around 10 s of simulation time to reach near steady-state conditions as the biomass and the fuel is fed to a heated standstill reactor at time t = 0 s.

However, the carbon conversion depends upon different factors such as the reactant gas distribution inside the gasifier, fluid velocity, mixing, etc. Particles in the central region have a higher probability of easy access to gasifying agents such as oxygen. The conversion of the char inside the gasifier is affected by the fluid velocity and direction inside the reactor. Fig. 7 shows the instantaneous fluid velocity distribution.

As depicted in the figure, recirculation of mostly occurs around the wall of the reactor. Whereas, in the central region the fluid velocity increases gradually with descending gasifier elevation. The recirculation and rapid gas expansion are due to the expansion mechanism of the injection nozzles. The expansion in a radial direction is high compared to the axial direction due to the high jet velocity along the axial direction. This agrees well with the results published by Liang et al. (Liang et al., 2020), where the reactor consists of a zone of recirculation, spreading, and fast-flowing. The flow vector is nearly random throughout the reactor with exception in the middle of the reactor. This behavior of the entrained flow reactor has a great influence on the particle mixing and the overall conversion efficiency of the reactor. Further, the gas composition, reactor temperature, and reaction kinetics are analyzed during this study.

It is important to monitor the gas composition and the fluid temperature along the reactor. Fig. 8 gives the calculated parameters along with the height of the reactor. The cut-planes are at 0.2, 0.4, 0.6, 0.8, 1.0, 1.2, 1.4, 1.6 m from the bottom of the reactor. The figure shows the instantaneous mole fraction of CO, H_2, and CO_2 and the average fluid temperature (K) at t = 50 s. As shown in Fig. 8 (d), the average fluid temperature of the reactor gave a radial profile at the outlet, which shows that homogeneous mixing in the

Table 5
Comparison between the simulation and experimental results.

		CH_4	CO	CO_2	H_2	Syngas mass flow, dry basis (kg/h)
Simulation	mol %[1]	3.8	45.7	22.6	27.5	76.3
	mol/kg fuel[2]	3.7	25.5	8.0	213.1	
Experiment	mol %	2.7	48.5	21.1	27.8	74.6
	mol/kg fuel	2.42	26.5	7.1	210.6	

[1]Dry, N_2 free basis.
[2]Back calculated by the authors for this article as no such calculations are present in the referred article.

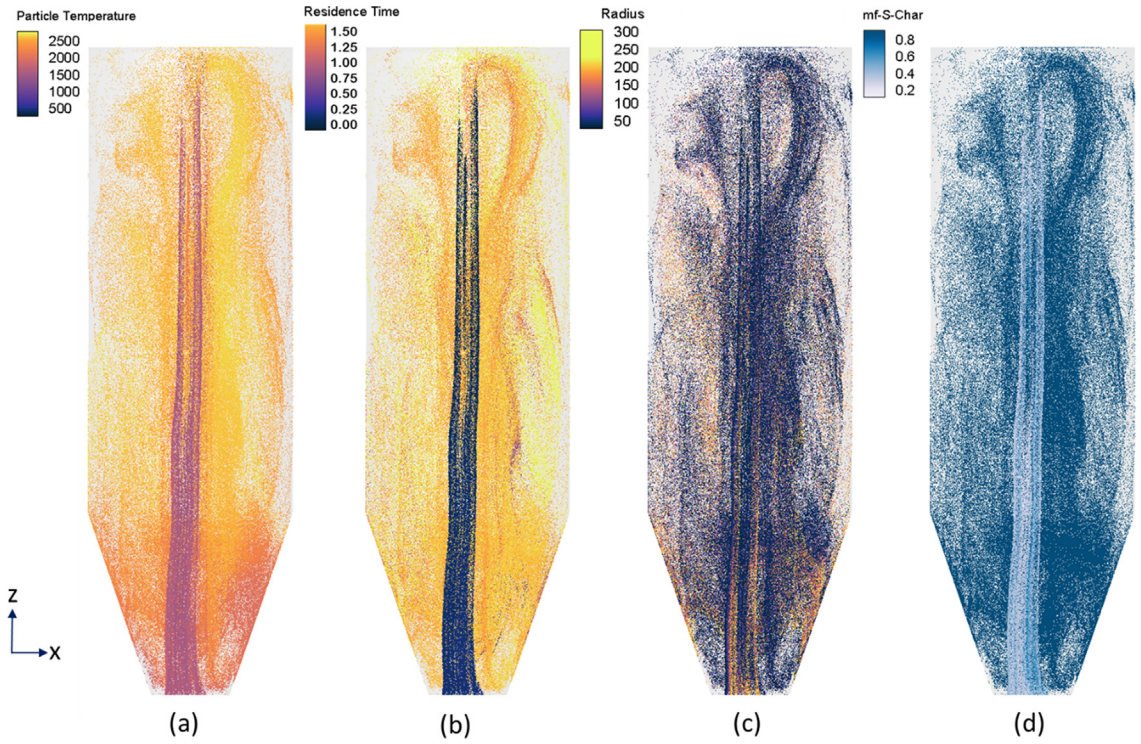

Fig. 5. The instantaneous distributions of particles with respect to (a) temperature (b), residence time (c) particle radius, and (d) carbon content at 50.0 s.

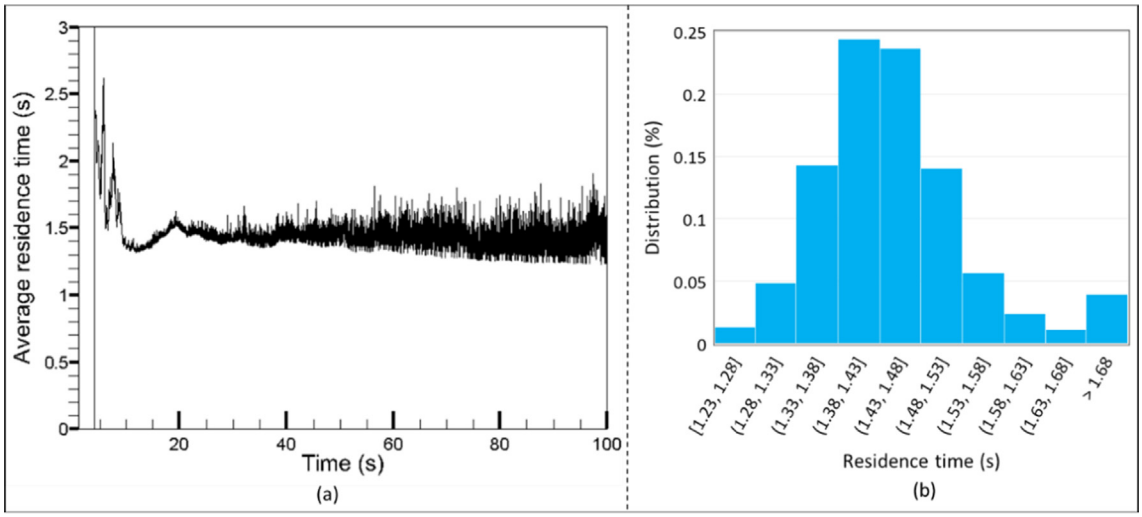

Fig. 6. (a) Average residence time for all particle species (b) Distribution percentage of the residence time in an interval of 0.05 s.

EF reactor is not achieved even at the exit areas. This is due to the fact that the majority of the particles are flowing through the central path where the majority of chemical reaction takes place and they take heat from the surroundings. Therefore, the central radial path has a lower temperature as compared to other regions in the radial direction.

The figures show the illustrative three-dimensional view of the gasifier during its operation. The bottom plane of the reactor gives the product gas from the reactor. The numerical values of the gas compositions and the reactor temperature are presented in Fig. 9. The gas compositions and the temperature are radially averaged at t = 50 s. Fig. 9 (b) shows the highest fluid temperature at the reactor injection burner. Analyzing the product gas composition and the temperature profile, combustion prevails around the burner region of the gasifier. Combustion supplies the necessary thermal heat for the other endothermic gasification reactions and the devolatilization of the biomass. There are no significant amounts of oxygen in the reactor. The oxygen concentration is 89 mol% in the injection burner and is completely consumed as it leaves the burner. Combustion in this region is the major reason for the peak fluid temperature.

As the chemical and thermal behavior are coupled together, a change in one affects the changes in the other one. Heat is supplied from walls as well as from the gas feed. Chemical transformation such as breaking chemical bonds gives sensible thermal energy, which changes the temperature. Gasification and combustion con-

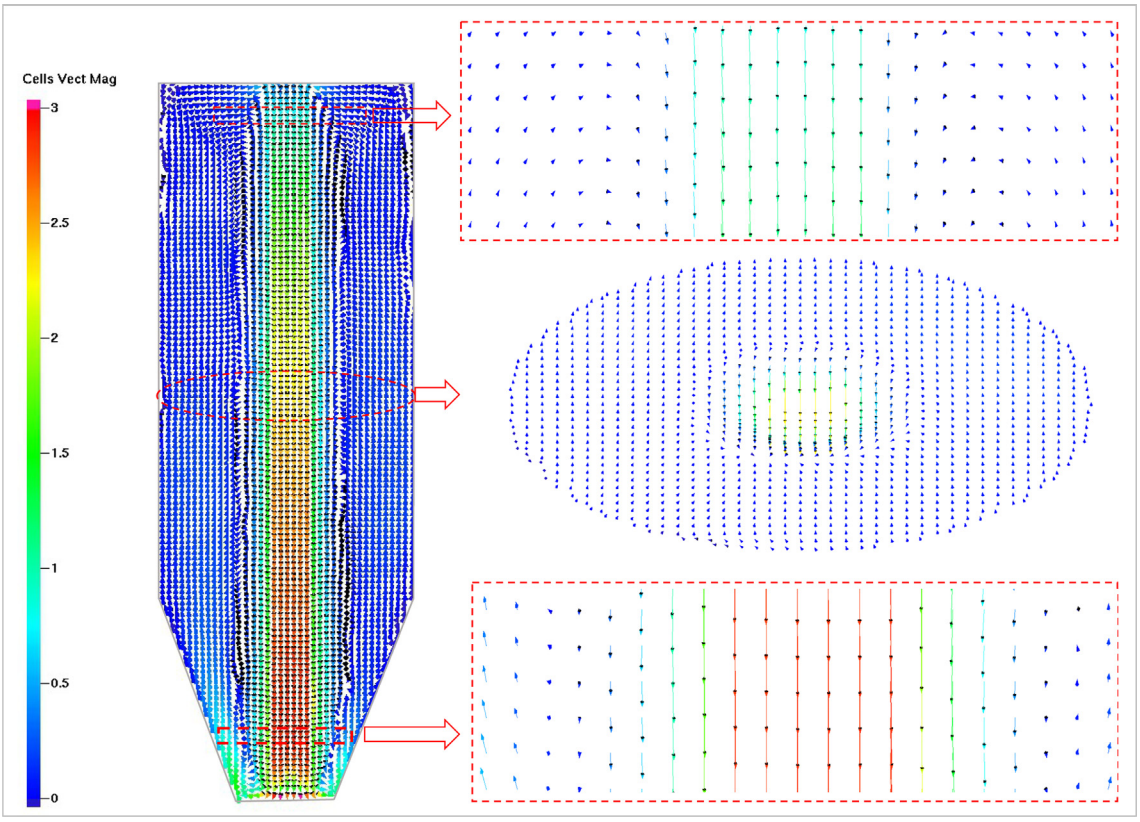

Fig. 7. Gas speed distribution at t = 50 sec.

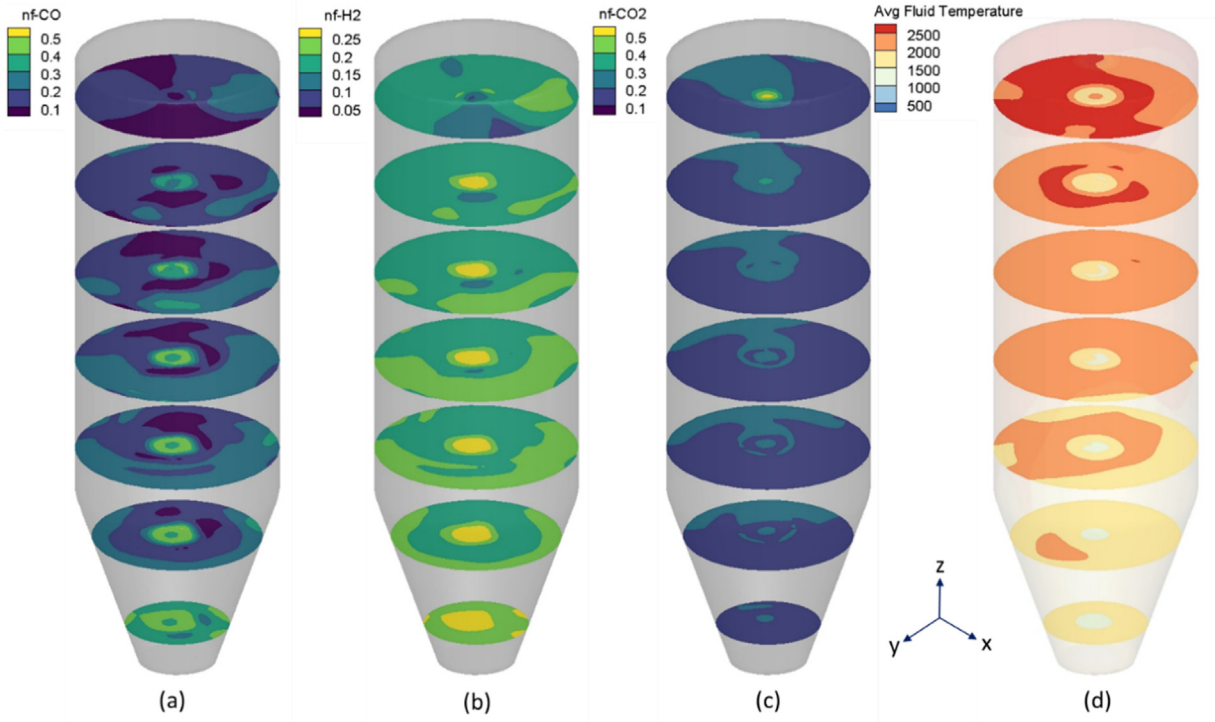

Fig. 8. Gasifier parameters at different levels in the reactor: Instantaneous mole fraction for gas species: - (a) CO, (b) H_2, (c) CO_2 and (d) time average fluid temperature.

sume and produce sensible heat respectively. Char gasification requires an optimal gas–solid contact; however, the conversion is sophisticated by the local variation in gas and temperature, depicted in Fig. 5 (a).

Chemistry affects the reactor dynamics by changing the gas composition and the reactor temperature. The above listed six chemical reactions were computed for each computational cell at each computational time step giving a transient 3D reactor behav-

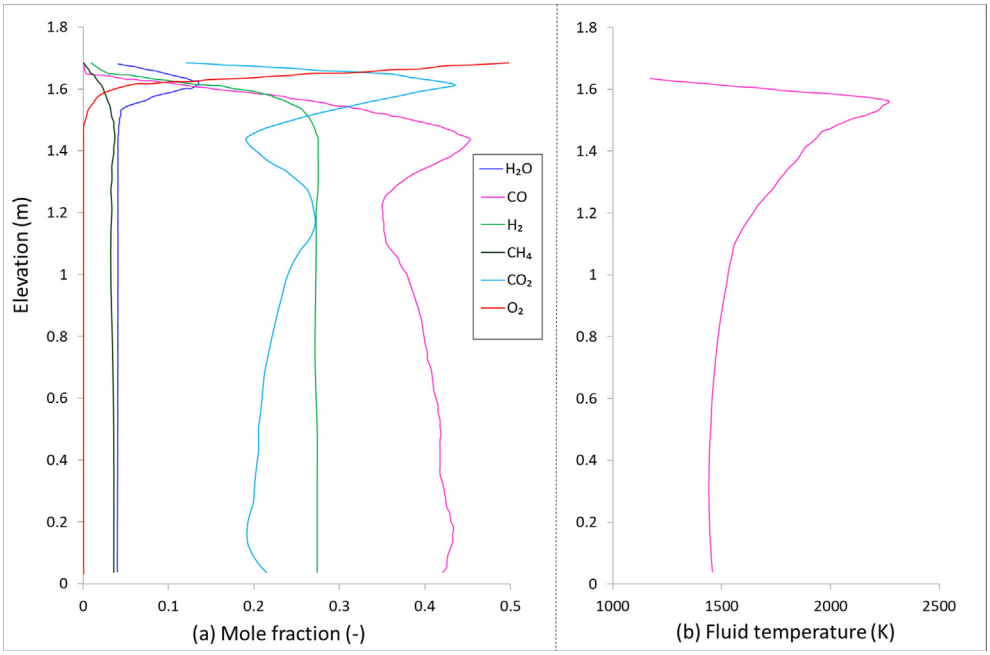

Fig. 9. (a), gas compositions (mole fraction) (b), fluid temperature versus elevation. Gas species and the fluid temperature are radially averaged.

ior. Fig. 10 shows the radially averaged reaction rates along with the gasifier depth. The figure shows that the reaction rates for different reactions are in the range of several orders of magnitude. As seen from Fig. 9 (a), CO is the dominant gas species throughout the reactor. As the reactor temperature is high around the fuel injector and the endothermic nature of the water gas shift reaction favors the forward reaction, the production of CO_2 is high in that region. The reaction rate decreases significantly for R04 with increasing reactor depth due to the decrease in reactor temperature and the small amounts of steam concentration as shown in Fig. 9 (a). Production of steam is from the oxidation of H_2 (R02), which significantly decreases with the reactor depth. This also limits the reaction rate for R04. The reaction rate for the R03 reaction is slow throughout the reactor elevation due to the fact that the CH_4 is present at a low concentration compared to the other gases in the reactor. The dominant methane production source is the devolatilization step, whereas the methanation reaction is not considered during this study due to its slow reaction rate.

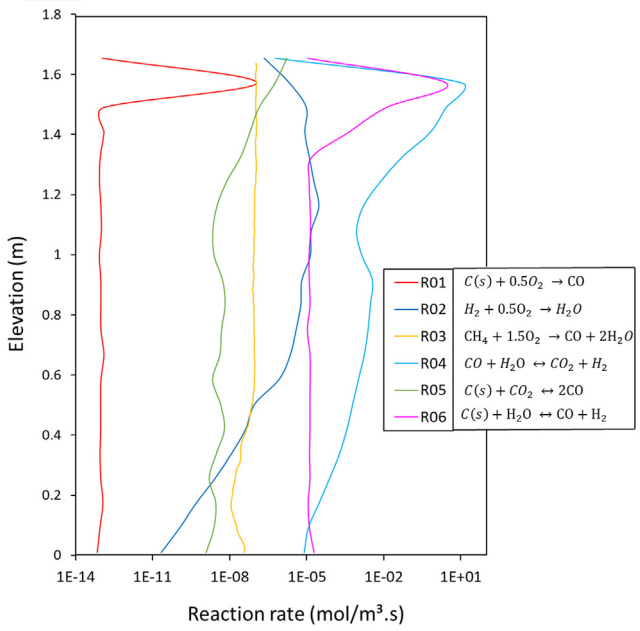

Fig. 10. Chemical reaction rate versus elevation at t = 50 s. Reaction rates are shown on a logarithmic scale.

Char oxidation (R01) is significant in the high-temperature region and all available oxygen is consumed around the fuel injector region. This gives the sufficiently low reaction below the fuel injector region. The char-steam reaction (R06) is also significant in the reactor entrance region, due to the presence of H_2O in this region. The majority of steam production in this region is from the reaction R02. The produced steam is quickly consumed by the reaction R06, as depicted by the mole fraction of H_2O in Fig. 9 (a).

The average mass production rate of the product gas was found to be 0.022 kg/s. As the product gas was produced at a high temperature, the ideal gas law was applied to calculate the gas production rate at normal temperature and pressure conditions (25 °C and 1 atm). The ratio of product gas to biomass was calculated as 3.61 Nm^3/kg of biomass. The average gas fractions on a volume basis were 0.038 of CH_4, 0.457 of CO, 0.226 of CO_2, and 0.275 of H_2. The lower heating value of the product gas is calculated as 7.8 MJ/kg. The carbon conversion efficiency was calculated as 99.1 % based on the amount of carbon converted into product gases using the formula $[(1 - m_{char})/(m_{biomass} \cdot \%C)] \cdot 100\%$. The lower heating values for the product gas components are taken from the literature (Waldheim & Nilsson, 2001). The CGE of the gasifier is calculated as 61.3% using equation (26):

$$\mathrm{CGE} = \frac{\dot{m}_{gas}(kg/s) \cdot LHV_{gas}(MJ/kg)}{\dot{m}_{fuel}(kg/s) \cdot LHV_{gas}(MJ/kg)} \tag{26}$$

3.2. Effect of temperature

The effect of reactor temperature on the product gas was analyzed for the initial reactor temperature of 1000℃, 1100℃, 1200℃, and 1300℃. The time taken to reach the near steady-state condition decreased with an increase in reactor temperature.

The time taken to reach close to the steady-state increased from around 8 s to around 13 s as the reactor temperature increased from 1000℃ to 1300℃. Changes in the reactor temperature change the reaction rate and the time to reach the equilibrium/steady state. The product gas composition is the average value obtained from the reactor output.

Fig. 11 shows the product gas composition at four different reactor temperatures. With an increase in reactor temperature, the concentration of CO and H_2 increased slightly, whereas the concentration of CO_2 and CH_4 decreased slightly. Increasing the reactor temperature gave changes in the product gas composition, as illustrated in the figure. The predicted gas compositions are consistent with the experimental results of coal gasification published by Lee et al. (Lee et al., 1996). Therefore, it is crucial to study the reactor parameters to optimize reactor performance.

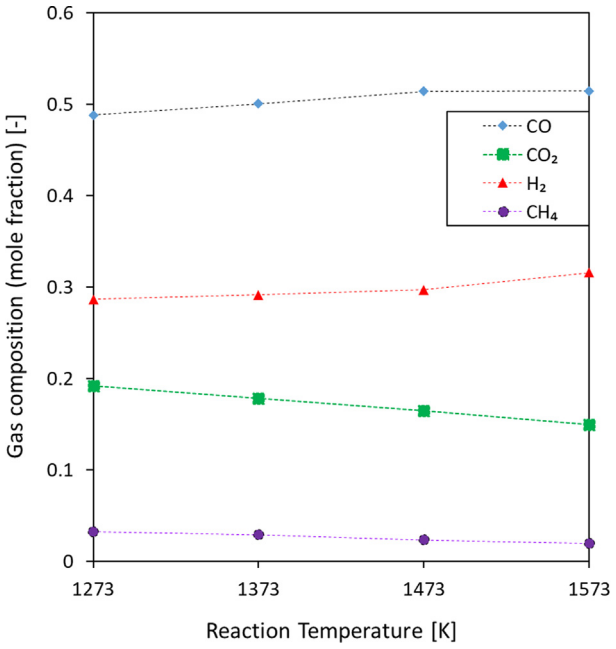

Fig. 11. Product gas composition at four different reactor temperatures (dry basis).

3.3. Effect of equivalence ratio

The effect of the oxygen equivalence ratio was simulated and analyzed for the developed model. The change in the oxygen supply changes the chemistry inside the reactor, which in turn affects the hydrodynamics inside the reactor. The variation of equivalence ratio (λ) is presented in Fig. 12. The product gas in the figure is presented on a dry, N_2 free basis.

The optimal gasification performance (higher mole fraction of CO and H_2) is in the range of equivalence ratio 0.3 to 0.44. An increase in the equivalence ratio above 0.6 gave oxygen in the product gas particularly due to short residence time for these types of gasifiers. The char in the product gas is consumed almost 100% for the equivalence ratio greater than 0.3. The higher the equivalence ratio the higher the reaction rates for combustion reaction thereby increasing the process temperature. For more parametric variations and variations of process conditions, interested readers are advised to read the results published by Weiland et al (Weiland et al., 2015).

4. Conclusion

This study investigated the biomass gasification behaviors in an entrained flow reactor by developing a simulation model based on the MP-PIC approach. The model is validated against the results from an experiment published in the literature. The results suggest the suitability of the model for multiphase systems such as EF reactors. The gasifier performance is quantified based on the results obtained from the model. The model gave a good prediction of the gasifier behavior and its chemistry, which can be used to optimize entrained flow reactors. The main focus was to evaluate the product gas composition, the reaction kinetics, and the flow behavior inside the gasifier. Simulations showed that the CPFD is an excellent tool to predict the gasification behavior inside an entrained flow reactor. The overall efficiency (or CGE) of industrial-scale entrained flow reactors is expected to be higher than for the pilot-scale reactor due to the lower ratio of thermal heat losses to fuel input.

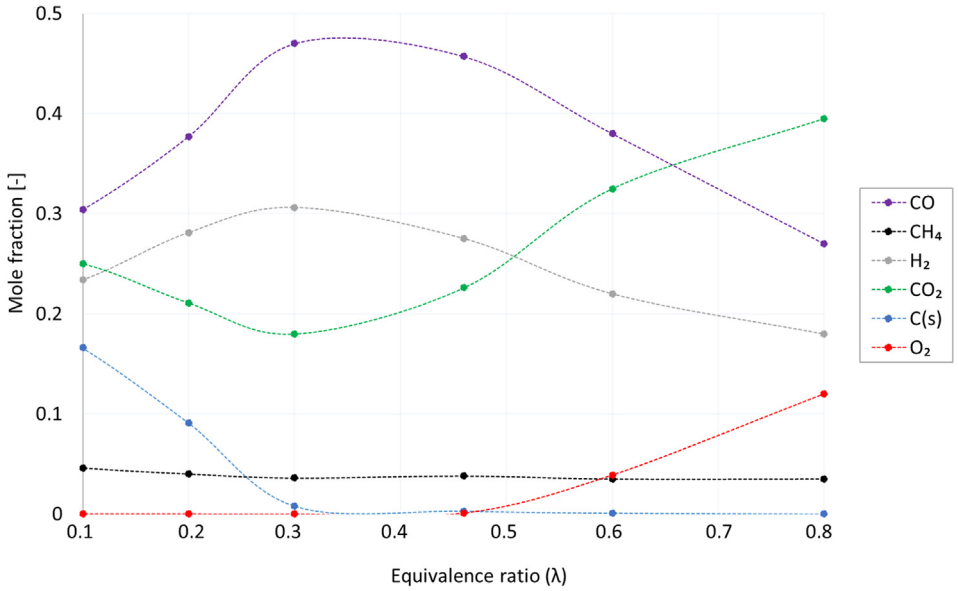

Fig. 12. product gas composition at a different equivalence ratio (dry basis).

Char oxidation is significant in the high-temperature region, whereas the char-CO_2 reaction is prevalent throughout the reactor depth. The endothermic nature of the water gas shift reaction favors the high production of CO_2 in high-temperature regions and its reaction rate decreased significantly with reactor depth. Simulations show the zones of high and low-temperature regions, suggesting different reaction zones such as a partial combustion zone near the fuel injector followed by a gasification zone. Change in the operational temperature from 1000℃ to 1300℃ gave an increase of 12.45% of CO and 17.5% of H_2 and a decrease of 34.55% of CH_4 and 17.15% of CO_2 on a dry nitrogen-free basis. At a lower equivalence ratio, some amounts of char were present in the product gas whereas, at a higher equivalence ratio, O_2 was present in the product gas. However, there are some uncertainties in these results. Simulation of the complete system including the feeding system as well as the quench bath for gas cooling and the inclusion of tar and slag, will overcome the uncertainties to a certain extent in this study.

CRediT authorship contribution statement

Ramesh Timsina: Conceptualization, Writing – original draft, Validation. **Rajan K Thapa:** Software, Investigation, Supervision. **Britt M.E. Moldestad:** Supervision, Writing – review & editing. **Marianne S. Eikeland:** Supervision, Writing – review & editing.

Declaration of Competing Interest

The authors declare that they have no known competing financial interests or personal relationships that could have appeared to influence the work reported in this paper.

Acknowledgments

The authors would like to thank the University of South-Eastern Norway for providing the CFD package and the computer resources for the simulation. We would like to acknowledge the research center for environmental-friendly energy research (FME) Bio4fuels [Project number: 257622] for supporting this work. This research did not receive any specific grant from a funding agency in the public, commercial, or non -profit sectors.

Appendix A. Supplementary data

Supplementary data to this article can be found online at https://doi.org/10.1016/j.cesx.2021.100112.

References

Abani, N., Ghoniem, A.F., 2013. Large eddy simulations of coal gasification in an entrained flow gasifier. Fuel 104, 664–680. https://doi.org/10.1016/j.fuel.2012.06.006.

Abbasi, A., Islam, M.A., Ege, P.E., de Lasa, H.I., 2013. CPFD flow pattern simulation in downer reactors. AIChE J. 59 (5), 1635–1647. https://doi.org/10.1002/aic.13956.

Andrews, M.J., O'Rourke, P.J., 1996. The multiphase particle-in-cell (MP-PIC) method for dense particulate flows. Int. J. Multiph. Flow 22 (2), 379–402. https://doi.org/10.1016/0301-9322(95)00072-0.

Ariyaratne, W.H., Ratnayake, C., Melaaen, M.C., 2017. Application of the MP-PIC method for predicting pneumatic conveying characteristics of dilute phase flows. Powder Technol. 310, 318–328. https://doi.org/10.1016/j.powtec.2017.01.048.

Bandara, J.C., Moldestad, B.M., Eikeland, M.S., 2018. Analysing the effect of temperature for steam fluidized-bed gasification of biomass with MP-PIC simulation. Int. J. Energy Environ. 9 (6), 529–542.

Bandara, J.C., Thapa, R., Nielsen, H.K., Moldestad, B.M.E., Eikeland, M.S., 2021. Circulating fluidized bed reactors–part 01: analyzing the effect of particle modelling parameters in computational particle fluid dynamic (CPFD) simulation with experimental validation. Part. Sci. Technol. 39 (2), 223–236. https://doi.org/10.1080/02726351.2019.1697773.

Basu, P., 2018. Biomass gasification, pyrolysis and torrefaction: practical design and theory (Second ed.). London UK: Academic press (Elsevier).

Bates, R.B., Ghoniem, A.F., Jablonski, W.S., Carpenter, D.L., Altantzis, C., Garg, A., Barton, J.L., Chen, R., Field, R.P., 2017. Steam-air blown bubbling fluidized bed biomass gasification (BFBBG): Multi-scale models and experimental validation. AIChE J. 63 (5), 1543–1565. https://doi.org/10.1002/aic.v63.510.1002/aic.15666.

Bikane, K., Yu, J., Long, X., Paterson, N., Millan, M., 2020. Linking char reactivity to structural and morphological evolution during high pressure pyrolysis of Morupule coal. Chemical Engineering Science: X 8, 100072. https://doi.org/10.1016/j.cesx.2020.100072.

Chen, C.-J., Hung, C.-I., Chen, W.-H., 2012. Numerical investigation on performance of coal gasification under various injection patterns in an entrained flow gasifier. Appl. Energy 100, 218–228. https://doi.org/10.1016/j.apenergy.2012.05.013.

Chiesa, M., Mathiesen, V., Melheim, J.A., Halvorsen, B., 2005. Numerical simulation of particulate flow by the Eulerian-Lagrangian and the Eulerian-Eulerian approach with application to a fluidized bed. Comput. Chem. Eng. 29 (2), 291–304. https://doi.org/10.1016/j.compchemeng.2004.09.002.

Duchesne, M. A., 2012. Slagging in entrained-flow gasifiers. (Doctor Philosophiae). Université d'Ottawa/University of Ottawa. Retrieved from https://ruor.uottawa.ca/handle/10393/23353.

Eluk, T., Levy, A., Korytnyi, E., Bar-Kohany, T., 2017. Transition mechanism between combustion regions in swirling entrained flow downer reactors. Energy Fuels 31 (2), 1927–1934. https://doi.org/10.1021/acs.energyfuels.6b02225.

Gao, X., Zhang, Y., Bao, F., Li, B., Zhao, Y., Ke, C., Jiang, B., 2018. CFD modeling of sawdust gasification in a lab-scale entrained flow reactor based on char intrinsic kinetics. Part 1: Model development. Chemical Engineering and Processing-Process Intensification. 125, 280–289. https://doi.org/10.1016/j.cep.2018.02.017.

Gao, X., Zhang, Y., Li, B., Yu, X., 2016. Model development for biomass gasification in an entrained flow gasifier using intrinsic reaction rate submodel. Energy Convers. Manage. 108, 120–131. https://doi.org/10.1016/j.enconman.2015.10.070.

Gungor, A., Yildirim, U., 2013. Two dimensional numerical computation of a circulating fluidized bed biomass gasifier. Comput. Chem. Eng. 48, 234–250. https://doi.org/10.1016/j.compchemeng.2012.09.012.

Guo, N., 2020. Modelling of reacting multi-phase flow for biomass gasification. Doctor Philosophiae. Norwegian University of Science and Technology.

Guo, N., García Llamas, Á.D., Li, T., Umeki, K., Gebart, R., Løvås, T., 2020. Computational fluid dynamic simulations of thermochemical conversion of pulverized biomass in a dilute flow using spheroidal approximation. Fuel 271, 117495. https://doi.org/10.1016/j.fuel.2020.117495.

Harris, S., Crighton, D., 1994. Solitons, solitary waves, and voidage disturbances in gas-fluidized beds. J. Fluid Mech. 266, 243–276. https://doi.org/10.1017/S0022112094000996.

IEA., 2019. Global Energy & CO2 Status Report 2019. https://www.iea.org/reports/global-energy-co2-status-report-2019. (accessed 28 March 2021)

Ku, X., Li, T., Løvås, T., 2014. Eulerian–lagrangian simulation of biomass gasification behavior in a high-temperature entrained-flow reactor. Energy Fuels 28 (8), 5184–5196. https://doi.org/10.1021/ef5010557.

Ku, X., Wang, J., Jin, H., Lin, J., 2019. Effects of operating conditions and reactor structure on biomass entrained-flow gasification. Renewable Energy 139, 781–795. https://doi.org/10.1016/j.renene.2019.02.113.

Kumar, M., Ghoniem, A.F., 2013. Application of a validated gasification model to determine the impact of coal particle grinding size on carbon conversion. Fuel 108, 565–577. https://doi.org/10.1016/j.fuel.2013.02.009.

Lanza, A., Islam, M.A., de Lasa, H., 2016. CPFD modeling and experimental validation of gas–solid flow in a down flow reactor. Comput. Chem. Eng. 90, 79–93. https://doi.org/10.1016/j.compchemeng.2016.04.007.

Lee, J.G., Kim, J.H., Lee, H.J., Park, T.J., Kim, S.D., 1996. Characteristics of entrained flow coal gasification in a drop tube reactor. Fuel 75 (9), 1035–1042. https://doi.org/10.1016/0016-2361(96)00084-1.

Liang, Y., Guo, C.Y., Zhao, X., Qin, Q., Cheng, Y., He, L., 2020. CPFD simulation on particle behaviour in an entrained-flow gasifier. Clean Energy. 4 (1), 75–84. https://doi.org/10.1093/ce/zkz032.

García Llamas, Á.D., Guo, N., Li, T., Gebart, R., Løvås, T., Umeki, K., 2020. Morphology and volume fraction of biomass particles in a jet flow during devolatilization. Fuel 278, 118241. https://doi.org/10.1016/j.fuel.2020.118241.

Long, X., Spiegl, N., Berrueco, C., Paterson, N., Millan, M., 2020. Fluidised bed oxy-fuel gasification of coal: Interactions between volatiles and char at varying pressures and fuel feed rates. Chemical Engineering Science: X. 8,. https://doi.org/10.1016/j.cesx.2020.100068 100068.

Mu, L., Buist, K.A., Kuipers, J.A.M., Deen, N.G., 2020. Scaling method of CFD-DEM simulations for gas-solid flows in risers. Chemical Engineering Science: X. 6, 100054. https://doi.org/10.1016/j.cesx.2019.100054.

Nakhaei, M., Grévain, D., Jensen, L.S., Glarborg, P., Dam–Johansen, K., Wu, H., 2021. NO emission from cement calciners firing coal and petcoke: A CPFD study. Applications in Energy and Combustion Science. 5, 100023. https://doi.org/10.1016/j.jaecs.2021.100023.

Nakhaei, M., Hessel, C.E., Wu, H., Grévain, D., Zakrzewski, S., Jensen, L.S., Glarborg, P., Dam-Johansen, K., 2018. Experimental and CPFD study of gas–solid flow in a cold pilot calciner. Powder Technol. 340, 99–115. https://doi.org/10.1016/j.powtec.2018.09.008.

Nakhaei, M., Wu, H., Grévain, D., Jensen, L.S., Glarborg, P., Dam–Johansen, K., 2019. CPFD simulation of petcoke and SRF co–firing in a full–scale cement calciner. Fuel Process. Technol. 196, 106153. https://doi.org/10.1016/j.fuproc.2019.106153.

Qin, K. (2012). Entrained flow gasification of biomass. (Doctor Philosophiae). Technical University of Denmark. Retrieved from https://hdl.handle.net/11250/2650837.

Ren21., 2020. Renewables 2020 - Global status report. Retrieved from https://www.ren21.net/wp-content/uploads/2019/05/gsr_2020_full_report_en.pdf. (accessed 08 April 2021)

Sepman, A., Yngve, Ö., Zhechao, Q., Henrik, W., Florian, M.S., 2017. Real-time in situ multi-parameter TDLAS sensing in the reactor core of an entrained-flow biomass gasifier. Proc. Combust. Inst. 36 (3), 4541–4548. https://doi.org/10.1016/j.proci.2016.07.011.

Shi, X., Sun, R., Lan, X., Liu, F., Zhang, Y., Gao, J., 2015. CPFD simulation of solids residence time and back-mixing in CFB risers. Powder Technol. 271, 16–25. https://doi.org/10.1016/j.powtec.2014.11.011.

Smagorinsky, J., 1963. General circulation experiments with the primitive equations: I. The basic experiment. Monthly weather review. 91(3), 99-164. 10.1175/1520-0493(1963)091<0099:GCEWTP>2.3.CO;2.

Snider, D.M., Clark, S.M., O'Rourke, P.J., 2011. Eulerian-Lagrangian method for three-dimensional thermal reacting flow with application to coal gasifiers. Chem. Eng. Sci. 66 (6), 1285–1295. https://doi.org/10.1016/j.ces.2010.12.042.

Thapa, R.K., 2015. Optimization of flow behavior in biomass gasification reactor. Doctor Philosophiae. Telemark University College, Norway.

Thapa, R.K., Frohner, A., Tondl, G., Pfeifer, C., Halvorsen, B., 2016. Circulating fluidized bed combustion reactor: Computational Particle Fluid Dynamic model validation and gas feed position optimization. Comput. Chem. Eng. 92, 180–188. https://doi.org/10.1016/j.compchemeng.2016.05.008.

Thapa, R.K., Halvorsen, B.M., 2014. Heat transfer optimization in a fluidized bed biomass gasification reactor. Heat Transfer XIII: Simulation and Experiments in Heat and Mass Transfer. 83, 169. https://doi.org/10.2495/HT140161.

Timsina, R., Thapa, R.K., Moldestad, B.M., Eikeland, M.S., 2020. Experiments and computational particle fluid dynamics simulations of biomass gasification in an air-blown fluidized bed gasifier. International Journal of Energy Production and Management. 5 (2), 102–114. https://doi.org/10.2495/EQ-V5-N2-102-114.

Verma, V., Padding, J.T., 2020. A novel approach to MP-PIC: Continuum particle model for dense particle flows in fluidized beds. Chemical Engineering Science: X. 6,. https://doi.org/10.1016/j.cesx.2019.100053 100053.

Voultsos, I., Katsourinis, D., Giannopoulos, D., Founti, M., 2020. Integrating LCA with Process Modeling for the Energetic and Environmental Assessment of a CHP Biomass Gasification Plant: A Case Study in Thessaly, Greece. Eng—Advances. Engineering. 1 (1), 2–30. https://doi.org/10.3390/eng1010002.

Waldheim, L., Nilsson, T., 2001. Heating value of gases from biomass gasification. Retrieved from http://gasificationofbiomass.org/app/webroot/files/file/publications/HeatingValue.pdf.

Wang, Q., Niemi, T., Peltola, J., Kallio, S., Yang, H., Lu, J., Wei, L., 2015. Particle size distribution in CPFD modeling of gas–solid flows in a CFB riser. Particuology. 21, 107–117. https://doi.org/10.1016/j.partic.2014.06.009.

Weiland, F., Hedman, H., Marklund, M., Wiinikka, H., Öhrman, O., Gebart, R., 2013. Pressurized oxygen blown entrained-flow gasification of wood powder. Energy Fuels 27 (2), 932–941. https://doi.org/10.1021/ef301803s.

Weiland, F., Wiinikka, H., Hedman, H., Wennebro, J., Pettersson, E., Gebart, R., 2015. Influence of process parameters on the performance of an oxygen blown entrained flow biomass gasifier. Fuel 153, 510–519. https://doi.org/10.1016/j.fuel.2015.03.041.

Wu, Y., Shi, X., Liu, Y., Wang, C., Gao, J., Lan, X., 2020. 3D CPFD simulations of gas-solids flow in a CFB downer with cluster-based drag model. Powder Technol. 361, 400–413. https://doi.org/10.1016/j.powtec.2019.07.044.

Wu, Y., Zhang, J., Smith, P.J., Zhang, H., Reid, C., Lv, J., Yue, G., 2010. Three-dimensional simulation for an entrained flow coal slurry gasifier. Energy Fuels 24 (2), 1156–1163. https://doi.org/10.1021/ef901085b.

Ye, I., Ryu, C., 2015. Numerical modeling of slag flow and heat transfer on the wall of an entrained coal gasifier. Fuel 150, 64–74. https://doi.org/10.1016/j.fuel.2015.01.111.

Zhang, G.-Q., Ernst, L.J., de Saint Leger, O., 2000. Benefiting from thermal and mechanical simulation in micro-electronics. Springer, Netherlands.